

Highlights

Baffled tubes with superimposed oscillatory flow: experimental study of the fluid mixing and heat transfer at low net Reynolds numbers

J. Muñoz-Cámara, D. Crespí-Llorens, J.P. Solano, P. Vicente

- Flow visualization and convective heat transfer in oscillatory baffled reactors is studied
- The loss of axisymmetry and boost of mixing is found for $Re_{osc} > 130$
- The superimposed oscillatory flow increases heat transfer up to 4-5 times
- The relation between thermal stratification and flow oscillation is assessed

Baffled tubes with superimposed oscillatory flow: experimental study of the fluid mixing and heat transfer at low net Reynolds numbers

J. Muñoz-Cámara^a, D. Crespí-Llorens^b, J.P. Solano^a, P. Vicente^b

Published in *Experimental Thermal and Fluid Science* on 2021. DOI:10.1016/j.expthermflusci.2020.110324.

© 2023. Manuscript version under the CC-BY-NC-ND 4.0 license.

^aDep. Ing. Térmica y de Fluidos. Universidad Politécnica de Cartagena. Campus Muralla del Mar (30202). Cartagena (Spain).

^bDep. Ing. Mecánica y Energía. Universidad Miguel Hernández de Elche. Av. de la Universidad s/n (03202). Elche (Spain).

Abstract

Experimental results of flow pattern and heat transfer in circular-orifice baffled tubes under pure oscillatory flow and compound flow conditions are presented. The hydrogen bubble visualization technique is employed for describing the unsteady flow structure, and particle image velocimetry is used in order to measure the velocity field during eight different phases of the oscillation cycle. The existence of a central jet and the cyclic dispersion of vortices upstream and downstream of the baffles is analyzed. The loss of the flow axisymmetry for $Re_{osc} > 130$ is clearly identified. Heat transfer measurements under uniform heat flux (UHF) conditions are obtained in a thermal-hydraulic rig, allowing for the description of the influence of net and oscillatory Reynolds numbers on the Nusselt number, using propylene-glycol as working fluid ($Pr = 150$). The impact of chaotic mixing, for $Re_{osc} > 150$, results in a uniform local heat transfer distribution along the reactor cell, as well as in thermal uniformity in the transverse plane of the tube.

Keywords: Oscillatory baffled reactors, Flow mixing, Oscillatory flow, PIV, Heat transfer enhancement

Nomenclature

\dot{V} Volumetric flow rate

q'' Heat flux, W/m²

Q Heat, W

x_0 oscillation amplitude, center to peak (m)

t time (s)

T temperature (°C)

A_h heat transfer area (m²), πDL_h

c_p specific heat (J/(kg·K))

d orifice diameter (m)

D tube inner diameter (m)

f oscillation frequency (Hz)

k thermal conductivity (W/(m·K))

l cell length (m)

L_h heated length (m)

L_e length between the inlet temperature probe and the heated section beginning (m)

L_e length between the heated section end and the outlet temperature probe (m)

n_s number of interrogation windows

R_v axial-radial velocity ratio (-)

S open area (-), $(n \cdot d/D)^2$

u axial flow velocity (m/s)

U instantaneous bulk flow velocity (m/s), based on D

U_n bulk velocity of the net flow (m/s), based on D

v radial flow velocity (m/s)

x axial distance from the start of the heated area (m)

Greek symbols

μ dynamic viscosity (kg/(m·s))

ρ fluid density (kg/m³)

σ standard deviation

θ phase angle (°)

Subscripts

b bulk

e inlet of the heated section

in inlet of the test section

j section number

k circumferential position number

l lower position

o outlet of the test section

s outlet of the heated section

u upper position

w_i inner wall

amb ambient

L losses

Dimensionless groups

Re_n net Reynolds number, $\rho U_n D / \mu$

Re_{osc} oscillatory Reynolds number, $\rho(2\pi f x_0)D / \mu$

Ψ velocity ratio, Re_{osc} / Re_n

Pr Prandtl number, $\mu c_p / k$

Nu Nusselt number, hD / k

Ra^* Modified Rayleigh number, $q \rho c_p \beta D^4 q_p'' / (\nu k^2)$

1. Introduction

Heat transfer enhancement has attracted a significant degree of attention in the previous decades and still new techniques are being researched and developed. Traditionally, enhancement techniques have been classified [4] as active or passive, depending on whether or not an external power source is required.

Nowadays, active and passive combined techniques are gaining relevance [11, 1, 3], finding remarkable potential applications. This is the case of the Oscillatory Baffled Reactors (OBR) and their use for reactions with a high residence time [22], where the combined technique allows the flow to achieve a good mixing. A conventional continuous tubular reactor made of smooth tubes would require high Reynolds numbers to operate under turbulent flow conditions, which are needed to achieve good radial mixing. However, a high Reynolds number implies (for a given fluid and geometry) a high bulk velocity and, consequently, an extremely long tube in order to fulfil the high residence time requirement. An additional drawback would be the excessive pressure drop and pumping power. This problem is solved by using a combined technique: a set of equally-spaced baffles are introduced in the tube and an oscillatory flow is superimposed on a low net flow. This combination leads to a flow mechanism characterized by cyclic vortex dispersion upstream and downstream of the baffles. As a result, an augmentation of heat and mass transfer is achieved.

Flow patterns are one of the most studied aspects in OBRs. The aim is to identify the radial mixing mechanism and the influence of the operating conditions on

the onset of the flow asymmetry and the chaotic behaviour. The first noteworthy study dates from 1989, when Brunold et al. [5] tested several baffle spacings: $l = 1 - 2D$. They observed that the flow oscillation generates vortices downstream of the baffles during both oscillation half cycles, causing an intense mixing. The authors identified the optimal baffle spacing at $l = 1.5D$, a value which is currently a reference for the OBRs design.

Mackay et al. [15] performed the first study focused on the instability in OBRs. By using a qualitative flow visualization technique, the authors collected in a map the flow behaviour (asymmetric or not) as a function of the oscillatory Reynolds number, Re_{osc} , and the Strouhal number, St . The equations for both dimensionless numbers are included in the Nomenclature section. For the range of Strouhal numbers tested ($0.3 < St < 2$), the flow was asymmetric at an oscillatory Reynolds number of order 200.

During the past two decades there was a rise in the number of publications related to OBRs, introducing quantitative techniques such as CFD or PIV [21], in contrast with the qualitative visualization performed in previous studies. The main purpose of these studies was the study of the flow patterns, but with some chemical aspects as main goal, e.g., the scale-up [10], mixing and axial dispersion [18] or the viscosity effect on mixing [9]. It should be remarked that all of them were focused on the pure oscillatory flow, so they did not provide information about the net-oscillatory flow interaction.

Fitch et al. [9] studied the flow patterns in a baffled tube, for a range of $Re_{osc} = 6 - 5500$ and $St = 1.0$, using PIV and CFD. The authors found a 'channeling' effect with an inefficient vortex formation at very low oscillatory Reynolds numbers, $Re_{osc} = 6$, the symmetrical vortex formation at moderate intensities, $Re_{osc} = 20 - 150$, and the onset of an asymmetric flow at higher values, $Re_{osc} = 500 - 1000$. The effect of the flow patterns on the mixing was studied by the introduction of a new parameter, the axial-radial velocity ratio. This parameter took high values at low Re_{osc} , pointing out a poor mixing due to the prevalence of the axial component of the flow over the radial. The axial-radial velocity ratio decreases sharply with the oscillatory Reynolds number up to a value of ≈ 2 .

One of the studies mainly focused on the flow behaviour was performed by Zheng et al. [28]. The authors developed a 3D model, which was validated with PIV results. The model is used to obtain a two-dimensional map which shows the level of flow symmetry as a function of the Strouhal number and the oscillatory Reynolds number, i.e., pure oscillatory flow conditions. The authors observed that the maximum oscillatory Reynolds number at which the flow becomes asymmetric is 225, at a Strouhal number of 1.0. For $St < 0.5$, there is a reduction of the critical oscillatory Reynolds number. At $St = 0.1$ the asymmetry can be seen at $Re_{osc} = 100$. It is finally highlighted that, in spite of not

being a clear correlation, there is a connection between the flow asymmetry and the mixing intensity.

From the previous review, we can conclude that, while the OBRs have been widely studied, there are some relevant aspects of their performance that have not been properly addressed. That is the case of the flow patterns study in conditions with net and oscillatory flow (which is the common operating condition for the OBRs) or the study of the relation between flow asymmetry and mixing intensity and heat transfer.

Another aspect which has been a focus of attention since the OBRs conception is heat transfer. It has been motivated by the need of a right sizing of thermal circuits for heat addition or removal when endothermic or exothermic reactions take place in the OBR, or when the temperature is a key factor for the reaction.

Mackley et al. [17] studied heat transfer in a tube with equally-spaced one-orifice baffles. The range of dimensionless numbers tested was a Prandtl number of 124, a net Reynolds number, Re_n , between 100 and 700 and an oscillatory Reynolds number of 200-1600 (for a given net Reynolds number). The main conclusions were: 1) under steady flow conditions the baffles imply a significant heat transfer augmentation in comparison to a smooth tube, 2) under compound flow conditions (net and oscillatory flow) the effect of the oscillation on heat transfer was limited in the absence of baffles, while there was a significant increase for the baffled tube. Mackley and Stonestreet [16] extended the previous study, carrying out two experimental campaigns: the first focused on the study of the oscillating amplitude, and the second on the superposition of the net and the oscillatory flow. Regarding the amplitude, the effect on the Nusselt number was found to be moderate, with a slight increase for lower oscillating amplitudes (and the same maximum oscillatory flow velocity). The authors confirmed that an increase on the Re_n or the Re_{osc} imply a higher heat transfer rate. They found that at high net Reynolds numbers, i.e., when the velocity ratio Re_{osc}/Re_n is reduced, all the results converged to the steady flow results ($Re_{osc} = 0$). The research group P4G [23], from Cambridge University, studied the heat transfer in OBRs obtaining similar conclusions.

Law et al. [14] studied a similar OBR under cooling conditions and constant wall temperature. The tested ranges were: $Re_n = 200 - 1400$, $Re_{osc} = 0 - 2700$ and $Pr = 4.5 - 9$. The authors found that, for all the net Reynolds numbers tested, at high values of the oscillatory Reynolds number the Nusselt number converged to a given value. According to the authors, this observation could be related to the minimum axial dispersion observed by Smith and Mackley [24] in the range of oscillatory Reynolds numbers 800-1000. Above that range the radial mixing and the perturbation of the boundary layer would not rise.

Regarding the heat transfer studies pointed out in this introduction, the minimum net Reynolds number tested is of the order of 200, a value which has been identified

as the critical net Reynolds number for baffle inserts in recent studies [19]. Therefore, it would be interesting to extend the tested ranges to conditions where the net flow would be laminar and, consequently, there would exist a poor heat transfer under steady flow conditions.

This work presents a rigorous experimental study of a one-orifice baffled tube, using a set of experimental techniques which complement each other: hydrogen visualization and PIV. Besides, a thermohydraulic test rig has been used to characterise the heat transfer under uniform heat flux conditions. The study is focused on several points related to the heat transfer process and the interaction between the oscillatory and net flows at low net Reynolds numbers.

2. Experimental method

This section describes the facilities and experimental methods which have been used for this work. Three experimental methodologies have been employed: hydrogen bubbles flow visualization, particle image velocimetry, and heat transfer measurements. For that, two experimental facilities have been built: a visualization facility and a thermohydraulic testing facility.

The geometry under study, depicted in Fig. 1, consists of a tube with an inner diameter $D = 32$ mm and annular equally spaced insert baffles made of PEEK plastic, being their separation distance of $1.5D$ and the inner baffle diameter of $0.5D$. From now on, the space between consecutive baffles will be referred to as *cell tank*.

Different mixtures of water and propylene glycol are used as working fluid. The viscosity of the different fluid preparations has been measured to determine the exact ratio of water and glycol. The rest of the fluid thermophysical properties are deduced out of this ratio [2].

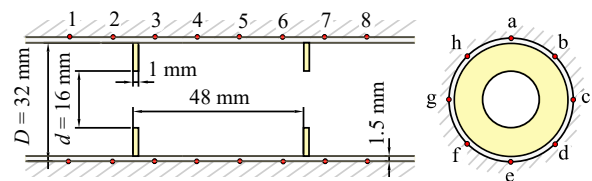


Figure 1: Baffle geometry and thermocouple arrangement in the test section.

2.1. Visualization facility

The facility depicted in Fig. 2a is used to perform visualization experiments under different working conditions. The working fluid is prepared in a reservoir tank (10), which is connected to a closed loop circuit. By the use of a chiller (8) connected through a plate heat exchanger (7) and an electric heater (11), the working fluid temperature is controlled. On the one hand, the system is built to generate a net flow through the test section (4) by using a centrifugal pump (1). On the other hand, a

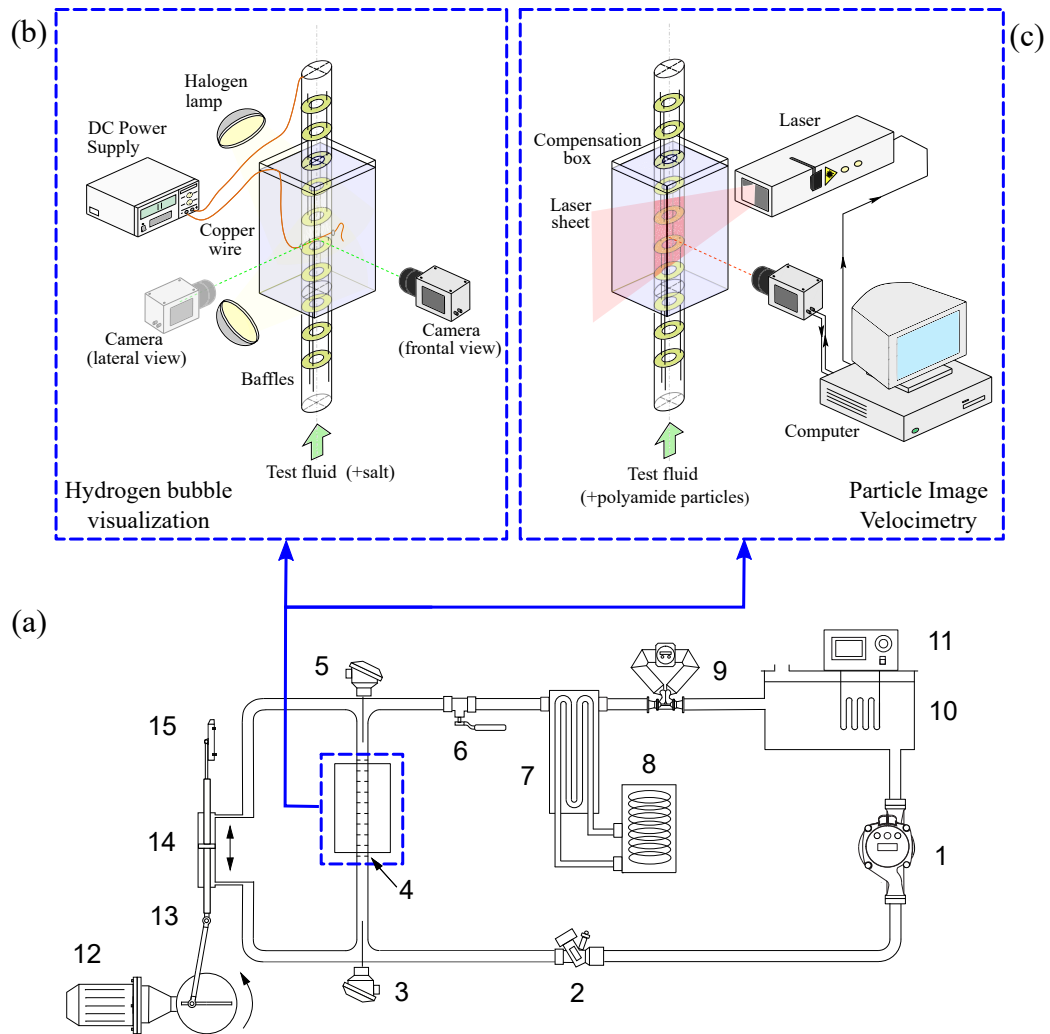


Figure 2: (a) Visualization facility, (b) image acquisition setup for hydrogen bubbles experiments and (c) PIV experiments. Visualization facility parts: (1) centrifugal pump, (2) flow control valve, (3) P100 inlet, (4) baffles, (5) PT100 outlet, (6) manual valve, (7) plate heat exchanger, (8) chiller, (9) Coriolis flowmeter, (10) reservoir tank, (11) electric heater, (12) gear-motor assembly, (13) connecting rod-crank, (14) hydraulic cylinder, (15) magnetostrictive position sensor.

hydraulic cylinder (14) is able to produce a 0.12 Hz to 1.2 Hz sinusoidal oscillatory flow in the test section (4). Both systems can be engaged at the same time, producing a compound flow: net and oscillatory. A flow control valve (2), has been used to ensure a stable net flow. The position of the hydraulic cylinder (14) is measured by a magnetostrictive position sensor (15). The visualization section (4) is surrounded by an acrylic box, which is filled with the working fluid and avoids image aberration.

In this facility, two visualization experimental techniques have been used: hydrogen bubbles and Particle Image Velocimetry (PIV), which are described in detail in the following sections. Flow field images for both type of experiments are captured by a 1280×1024 pix² CMOS IDT MotionScope M3 high speed camera.

2.2. Hydrogen bubble visualization

The configuration used to perform hydrogen bubbles experiments is depicted in Fig. 2b. A copper wire is inserted along the cross section diameter of the test tube, so that the symmetry plane containing the wire and the tube axis will be seeded with bubbles. For that, salt is dissolved in the fluid ($\sim 2 \text{ g/dm}^3$), and a voltage difference is produced between the formerly mentioned copper wire and a metallic accessory of the pipe loop, downstream the test section. The velocity of bubbles generation is adjusted by controlling the DC voltage difference ($0\text{-}12V_{\text{DC}}$) provided by a power source (BLAUSONIC FA-350). Illumination to the flow is provided by two 55 W halogen lamps. Fig. 2b shows two possible positions of the camera. One shows a *frontal view* of the seeded plane, and provides most of the information of the flow field. The other shows a *lateral view* of the seeded plane, and allows us to detect significant velocities in transverse direction to the symmetry plane.

2.3. Particle Image Velocimetry

The configuration used to perform PIV experiments is depicted in Fig. 2c. To this aim, the flow is seeded with $57 \mu\text{m}$ polyamide particles with a density of 1051 kg/m^3 . The symmetry plane is then illuminated by a 1 mm thick laser light sheet of 808 nm wavelength (200 Watts class IV Oxford laser with 0.15 mJ to 15 mJ per pulse). By taking two consecutive images of the seeded flow with the Motionscope M3 camera, and knowing the time elapsed between shots, the flow velocity pattern can be obtained by the PIV algorithm.

PIV is carried out by using the PIVlab code, version 2.31, for Matlab [27]. After PIV image pre-processing (histogram equalization, intensity highpass and intensity capping), 97.7% of the velocity vectors are found valid, $PPR > 2$ (peak-to-peak ratio). Image processing is carried out by the adaptive FFT (Fast Fourier Transform) cross correlation algorithm in four steps, where the last interrogation area size is $24 \times 24 \text{ pix}^2$. Post-processing includes the application of a global filter and two self-developed local filters, which are based on the

signal-to-noise ratio and on repeatability of the results across image pairs representing equivalent flow fields.

The time step between consecutive images to measure the whole oscillation cycle was chosen cautiously. The problem is that only one time step can be selected, but, at the same time, the flow shows very dissimilar velocities both in space and time during the cycle. The criterion was the following: ensuring that $PPR > 2$ for at least a 90 % of the velocity vectors for the phase with a maximum instantaneous bulk fluid velocity, $\theta = 90^\circ$, and this time step is used during the whole cycle.

2.3.1. Determination of the initial phase. Instantaneous flow rate calculation

The initiation of the images acquisition is triggered by a photoelectric sensor (OMROM E3JM). Nevertheless, deviations from the exact position or delays in the photoelectric sensor signal can lead to a wrong estimation of the cycle beginning (initial phase). In order to improve the determination of the initial phase, a PIV based instantaneous flow rate estimation is used.

A discretization of the integral expression of the flow rate assuming axisymmetric flow, $\dot{V} = \int_0^{0.5D} u(r) 2\pi r dr$, as a function of the velocity across its cross section is used to obtain the instantaneous flow rate. To that aim, the OBR test section is divided in a center circle and a series of annular spaces with the same width, given by the PIV algorithm interrogation area (IA) size. Each annular space, i , has a width $d_i = D/(2 n_d)$, where n_d is the number of IA in the radial direction. Thus, the axial velocity, u_i , is known for several radial positions, r_i , from $r = 0$ to $r = D/2$. r_i is given by the position of the IA center. The flow rate is then estimated by numerical integration,

$$\dot{V} = \sum_{i=1}^{n_d} u_i A_i = \frac{\pi}{4} \sum_{i=1}^{n_d} u_i \left[\left(r_i + \frac{d_i}{2} \right)^2 - \left(r_i - \frac{d_i}{2} \right)^2 \right] \quad (1)$$

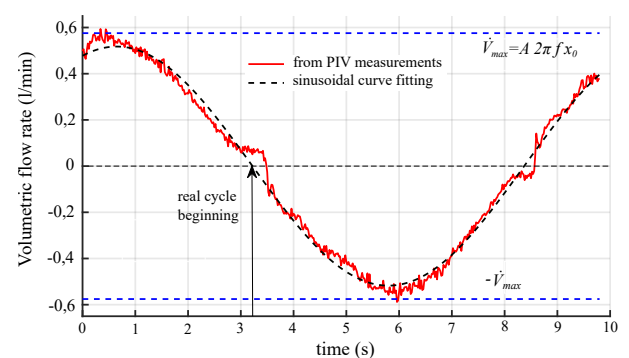


Figure 3: Instantaneous volumetric flow rate obtained from the PIV velocity field.

Fig. 3 shows the volumetric flow rate evolution throughout an oscillation cycle for a test with pure oscillatory flow. As a reference, the maximum and minimum theoretical flow rates, derived from the measured

oscillation amplitude and frequency, are also plotted. The maximum experimental values are close to the theoretical values, within a range of 10%. As can be observed, the waveform is mainly sinusoidal with a moderate noise level and the highest deviations are obtained around the null mean velocity point.

The previously mentioned deviations require a deeper analysis. They have been observed consistently over all the oscillation cycles, so they cannot be due to random errors related to the PIV technique. A more detailed observation of the measured instantaneous position of the piston revealed that the motion was not perfectly sinusoidal, but with a plateau and a more abrupt change in position at the end of the strokes. After deriving the instantaneous velocity (and then the flow rate) from the position signal with a numerical approximation, the flow rate shows a waveform which is very similar to that obtained from the PIV measurements. So, we can conclude that the deviations of the flow rate are generated by the imperfect (not sinusoidal) movement of the piston.

The previous methodology is only valid when the flow is axisymmetric, i.e., the axial velocity at each radial position can be considered as representative of the associated annular space. For the asymmetric case, the phase-averaged instantaneous flow rate has been used: a total of 20 cycles have been analysed and the averaged flow rate calculated for each phase of the cycle.

However, the flow rate curve obtained with this method has a noticeable noise level. Thus, if the raw signal were used to calculate the cycle beginning the results would be inaccurate. Instead, raw data are fitted to a sinusoidal curve. The zero crossing of this curve is considered as a better approximation for the cycle beginning. In Fig. 3 the sinusoidal fitting and the estimation of the cycle beginning are presented as well.

2.4. Heat transfer facility and methodology

A specific facility has been built for heat transfer tests (Fig 4). The main loop contains a reservoir tank (1), a Coriolis flowmeter (3) and a gear pump assembly (2) consisting of three pumps in parallel. The pumping system circulates the working fluid through a 32 mm diameter AISI 316 stainless steel tube (5), where the test section is located. Equally spaced insert baffles are arranged through the test section. Input and output temperatures are measured by two PT100 temperature probes (4, 7). A uniform heat flux is provided to the fluid by Joule effect, using a transformer and an auto-transformer (10) connected to the steel tube upstream and downstream of the test section. The separation distance between electrodes is $L_h = 26D$ mm. A secondary loop, which has been described in a previous work [19], is in charge of fluid temperature control. The whole facility and specially the test section are properly insulated.

As in the visualization facility, the sinusoidal oscillatory flow in the test section is generated by a rod-crank

mechanism (12, 13) attached to a double effect piston (11), which is connected in parallel to the test section. A magnetostrictive sensor (14) is used to determine the position of the piston. The assembly is capable of creating an oscillatory flow with a frequency ranging from 0.47 to 4.7 Hz.

In order to measure the tube wall temperature, a total of 8×8 type T thermocouples are attached to the steel tube outer diameter at 8 axial positions, each containing 8 thermocouples equally spaced around the tube cross section (see Fig. 1). As can be observed in Fig. 5, the 8 test sections are located well downstream of the first electrode ($x_1 = 20D$), in order to ensure periodicity of the flow.

Fig. 5 is a schematic representation of the variables involved in the local and average Nusselt numbers calculation. The bulk fluid temperature can be estimated from the measurements of the inlet fluid temperature ($T_{b,i}$), the heat provided (Q) by the autotransformer and the estimation of heat losses ($Q_{L,e}$, Q_L , $Q_{L,s}$).

The estimation of the heat losses is done by considering the overall heat transfer coefficient, which considers the internal convection coefficient, the conduction through the stainless steel tube wall and the insulation material and the external convection coefficient (free convection with the air). The last is calculated with the correlation for horizontal tubes proposed by Churchill and Chu [6]. It should be pointed out that the magnitude of the estimated heat losses is of the order of 2% of the heat applied by Joule effect. In any case, the uncertainty in the calculation of the heat losses (a conservative 50%) has been considered during the uncertainty analysis.

The local Nusselt number at each testing cross section can be obtained as

$$Nu_j = \frac{q''}{T_{wi,j} - T_{b,j}} \cdot \frac{D}{k_j} \quad (2)$$

where q'' is the heat flux provided to the fluid, $T_{b,j}$ is the estimated bulk temperature of the fluid at this section, $T_{wi,j}$ is the mean inner wall tube temperature and k_j is the thermal conductivity of the fluid. The inner wall temperature is calculated using a one-dimensional conduction model [13]. Previously, a set of tests is performed to calibrate the thermocouples under isothermal conditions when they are placed on the tube [19]. Finally, the Nusselt number Nu is obtained as the average of local Nusselt numbers $Nu = \sum_{j=1}^8 Nu_j / 8$.

An uncertainty analysis has been performed following the procedure described by Dunn [7]. This method takes into account: (1) the systematic error, due to the accuracy of the sensors and the acquisition system, which is provided by the manufacturers; and (2) the random errors, related to the repeatability of the measurements, which is estimated using the standard deviation of the measurements. Finally, the propagation of the individual measurements uncertainties on the final results is calculated.

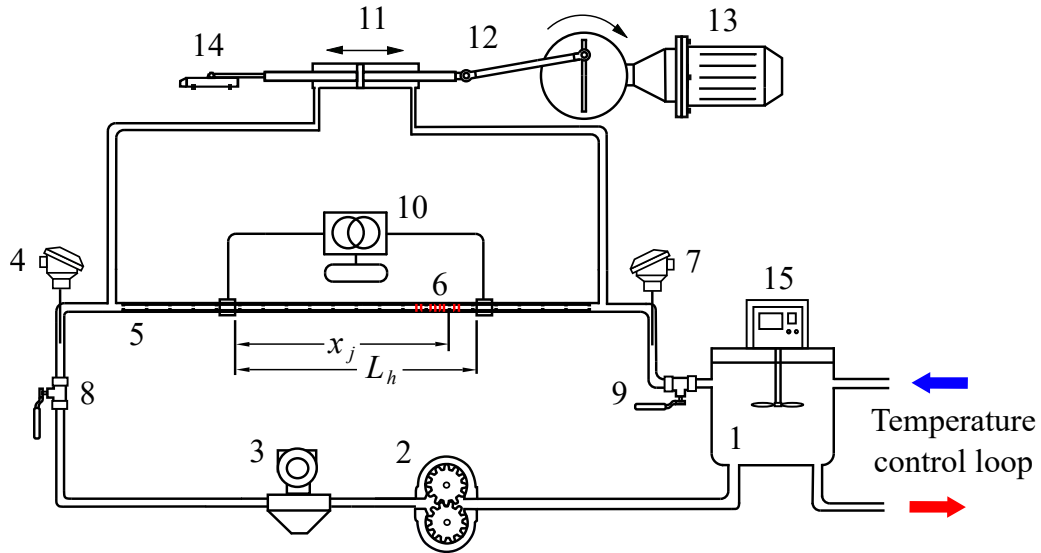


Figure 4: Heat transfer facility setup. (1) Main Tank, (2) positive displacement pumping system, (3) Coriolis flowmeter, (4) input flow temperature probe B 1/10 DIN PT100, (5) insert baffles, (6) type T thermocouples set, (7) output flow temperature probe, (8 and 9) manually operated valves, (10) autotransformer, (11) double effect hydraulic piston, (12) connecting rod-crank, (13) gear-motor assembly, (14) magnetostrictive position sensor, (15) agitator.

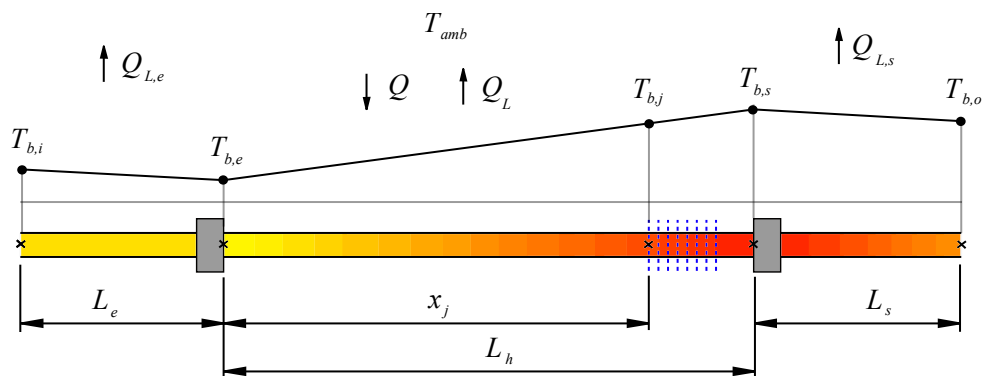


Figure 5: Temperature variation along the test section.

The experimental uncertainties, with a 95% confidence interval, derived from the previously described methodology are summarised in Table 1.

	Average	Maximum
Re_n	3.4%	4.9%
Re_o	4.2%	5.2%
x_0/D	2.0%	2.8%
Pr	3.3%	4.0%
Ra^*	5.2%	6.5%
Nu	7.1%	11.5%

Table 1: Uncertainties of results.

3. Results

This section presents the experimental results and analysis of the flow characteristics for the pure oscillatory flow and for the compound flow. The dynamic nature of the oscillatory flow makes it impractical to collect and/or present its full complexity throughout the entire oscillation cycle. Consequently, the results shown in this work for PIV measurements correspond to 8 equally spaced phases of the oscillation cycle, as shown in Fig. 6 (blue line). However, for a pure oscillatory flow and due to its temporal symmetry, the significant positions are reduced to 4. In addition, results for hydrogen bubble experiments are presented for significant cycle positions, but those with a higher image quality have been selected for presentation in the figures.

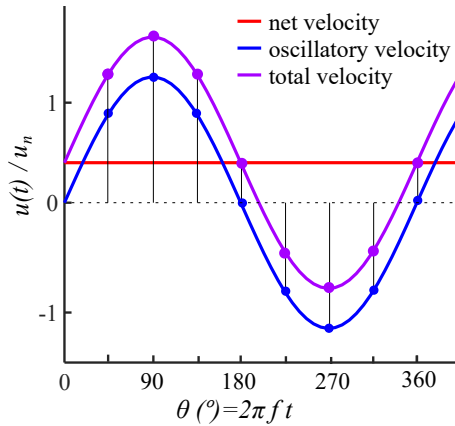


Figure 6: Phases of the oscillation cycle for flow field representation (PIV technique).

3.1. Oscillatory flow

Two types of visualization experiments have been carried out to analyse the flow behavior inside the device in conditions of pure oscillatory flow (nonexistent net flow). On the one hand, hydrogen bubbles experiments provide a qualitative evaluation of the flow conditions and a general overview of the full oscillation cycle. These experiments provide a valuable continuous observation of the oscillation cycle over time, which is,

as well, three dimensional. On the other hand, PIV experiments provide quantitative results of the flow pattern within the device for the most significant positions of the oscillation cycle. For this flow, the oscillatory Reynolds number is used, Re_{osc} .

3.1.1. Qualitative observation of the full cycle

Hydrogen bubbles experiments have been carried out for oscillatory Reynolds numbers ranging in $Re_{osc} \in [32, 160]$ and an oscillation amplitude of $x_0/D = 0.5$.

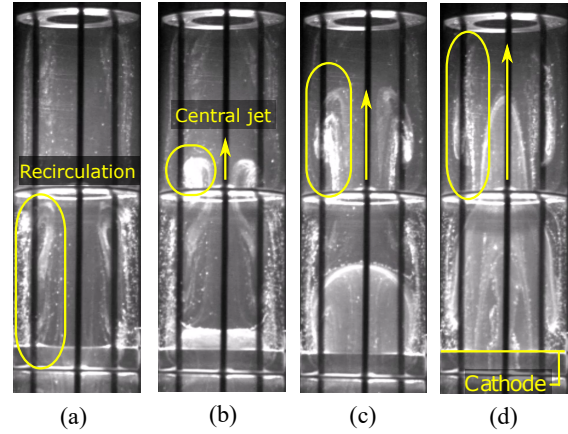


Figure 7: Front view of the hydrogen bubble seeded plane for $Re_{osc} = 32$. (a) $\theta = -22^\circ$, (b) $\theta = 22^\circ$, (c) $\theta = 55^\circ$ y (d) $\theta = 90^\circ$. $x_0/D = 0.5$.

Fig. 7 presents the visualization results for $Re_{osc} = 32$. Pictures show two consecutive cell tanks, being the copper wire (cathode) located at bottom of the lower tank. Fig. 7a shows the flow field just before the change of direction in the oscillation cycle. At this point, the downwards oscillation half cycle is about to finish and its recirculations can be observed. They are located in the peripheral fluid region, all along the cell tank. At Fig. 7b the flow field slightly after the new cycle beginning is shown. A contraction of the flow is observed upstream of the baffle, while downstream of it, a core jet with associated peripheral recirculations begins to develop. The structure has evolved in Fig. 7c to a mushroom shape, where the central jet and recirculations cover a longer fraction of the cell tank. Finally, at Fig. 7d the jet and the outer recirculations cover the full span of the cell tank, after which the flow will decelerate, and the same structure will be repeated in the opposite direction. These flow structures were previously visualized in the dye injection tests performed by Smith [25].

The front view of the flow field for $Re_{osc} = 150$ does not provide clear information about the influence of the oscillatory Reynolds number in this range, as significant deviations from the formerly commented case cannot be clearly identified. In order to observe further differences when varying the oscillatory Reynolds number, the same experiments are carried out for a different position of the camera. In this case, the flow plane which has

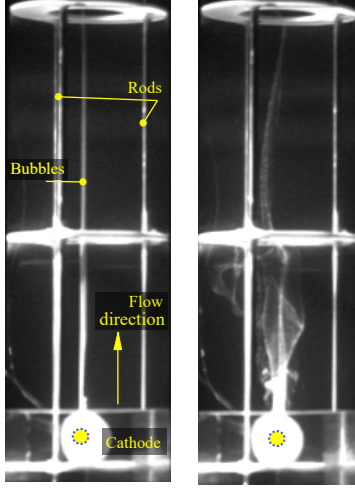


Figure 8: Lateral view of the hydrogen bubble seeded plane for instant $\theta = 180^\circ$, for (a) $Re_{osc} = 32$ y (b) $Re_{osc} = 150$. $x_0/D = 0.5$.

been seeded with hydrogen bubbles is observed from a lateral position (see *Lateral view* in Fig. 2b). From this perspective, the seeded plane in the two-dimensional image captured by the camera is observed as a straight line. Fig. 8 shows this view of the flow for $Re_{osc} = 32$ and $Re_{osc} = 150$. As can be seen, no velocity is detected in perpendicular direction to the seeded symmetry plane for $Re_{osc} = 32$. This allows us to conclude that the flow is axisymmetric, showing laminar characteristics all throughout the oscillation cycle. However, the behaviour is different for $Re_{osc} = 150$, where velocities in perpendicular direction to the plane are significant and they fluctuate across cycles, showing a much more complex and unstable nature of the flow.

[Front and lateral views of the flow for both oscillatory Reynolds numbers are presented in Video 1 for the full oscillation cycle. In this video, the development of the flow structures along the oscillation cycle is observed continuously and in detail. For example, the onset and evolution of the recirculation vortex and the central jet in continuous motion is key for the flow behaviour interpretation and shows details which cannot be fully appreciated by using PIV.] [Video 1 - Caption: Front and lateral views of the pure oscillatory flow for $Re_{osc} = 32$ and $Re_{osc} = 150$.]

The observed flow structure within the analysed range of oscillatory Reynolds numbers presents in any case significant momentum transfer in radial direction. This has two benefits for the use of this device as an OBR: flow mixing and heat transfer enhancement. However this qualitative technique does not allow us to quantify such benefits, other than that they seem to increase with the oscillatory Reynolds number. This point is addressed in the following sections.

3.1.2. Flow pattern

By using PIV, measurements and observations of the flow field have been carried out for oscillatory Reynolds

numbers within the range $Re_{osc} \in [30, 175]$ for $x_0/D = 0.5$.

In this section, instantaneous velocity fields obtained with PIV (Figures 9, 10) are scaled using the non-dimensional form u^+ , by dividing the instantaneous local velocity by the maximum instantaneous velocity of the field:

$$u^+ = \frac{|\vec{u}(r, x)|}{\max(|\vec{u}(r, x)|)} \quad (3)$$

This velocity u^+ is only used for PIV flow field representation purposes.

However, this non-dimensional form hides the differences in the bulk velocity between different cycle positions. To provide such information, velocity profiles are presented with a different non-dimensional velocity u^* .

$$u^* = \frac{u(r, x)}{2\pi f x_0} \quad (4)$$

where $2\pi f x_0$ is the maximum bulk velocity of the cycle, which occurs for the middle position of the piston $\theta = 90^\circ, 270^\circ$.

Firstly, the general characteristics of the flow are analysed as a function of the oscillatory Reynolds number. The results show two different flow regions which will be analysed.

On the one hand, in Section 3.1.1 the flow has been found to have laminar characteristics and to be axisymmetric for low Reynolds numbers. On the other hand, PIV results show that the flow pattern is periodic for the same range of Re_{osc} . This is observed in the flow patterns plotted in Figs. 9a and 9b at position $\theta = 180^\circ$ for $Re_{osc} = 51$. The figures present, respectively, the phase-averaged flow field and the instantaneous flow field at the same position of the cycle, showing no significant differences between them.

The results for $Re_{osc} > 130$ show a completely different behaviour. Figs. 9c and 9d show, respectively, the average and instantaneous flow fields at position $\theta = 180^\circ$ of the cycle for $Re_{osc} = 175$. As can be seen, there is no temporal periodicity across cycles and the instantaneous flow field (Fig. 9d) is asymmetric, showing recirculations which are not present in the phase-averaged field (Fig. 9c). This chaotic behaviour is also confirmed by the observations with hydrogen bubbles in Section 3.1.1. The critical value, for the onset of the asymmetric flow, was firstly measured as of the order of $Re_{osc} = 200$ (in the range $x_0/D = 0.04 - 0.035$), then by Smith [25] as $Re_{osc} = 150$ obtained (for an amplitude of $x_0/D = 0.04$) and, more recently, $Re_{osc} = 100$ at $x_0/D = 0.8$ by Zheng et al. [28]. Thus, in spite of the lack of results for the same dimensionless amplitude, we can conclude that the critical value of $Re_{osc} = 130$ is in good agreement with previous results.

Secondly, the flow field throughout the oscillation cycle is studied for the flow regimes which have been identified. Fig. 10a shows the most significant cycle positions $\theta = 0^\circ, 45^\circ, 90^\circ, 135^\circ$ for $Re_{osc} = 51$. These flow

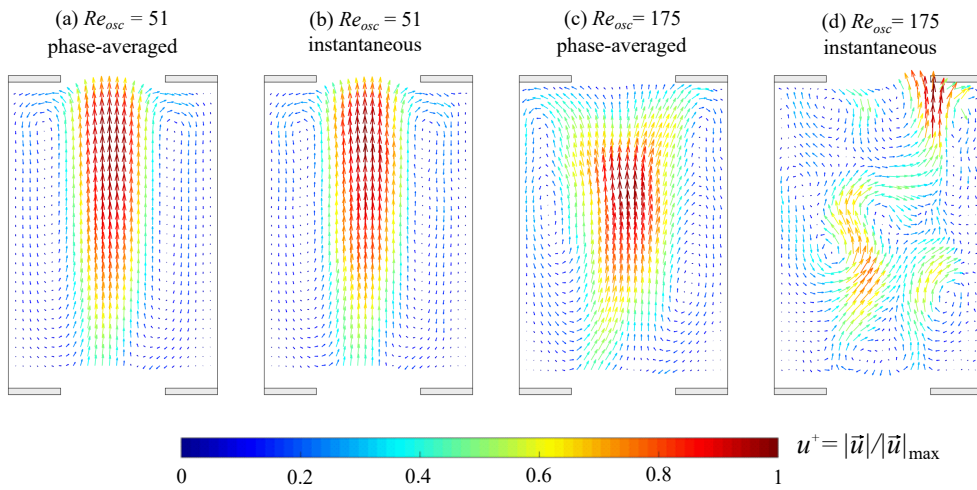


Figure 9: Phase-averaged vs. instantaneous velocity fields. Pure oscillatory flow

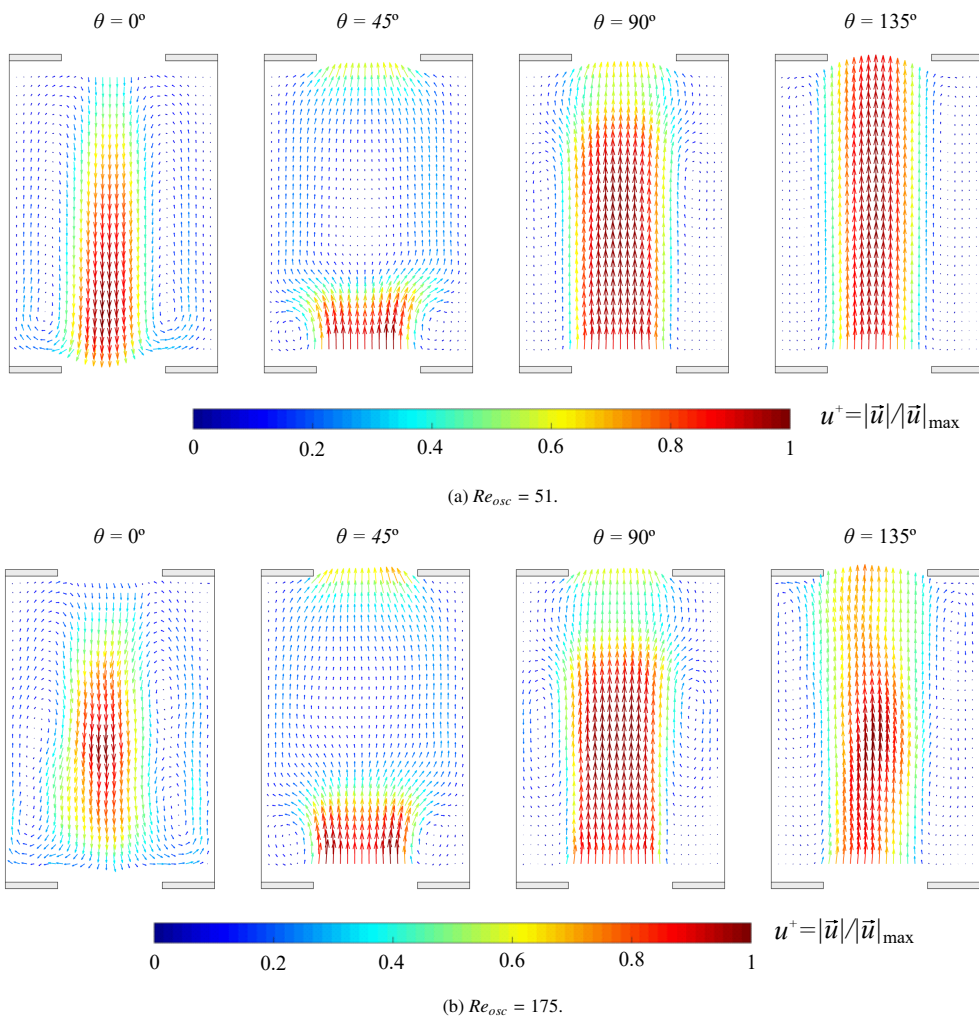
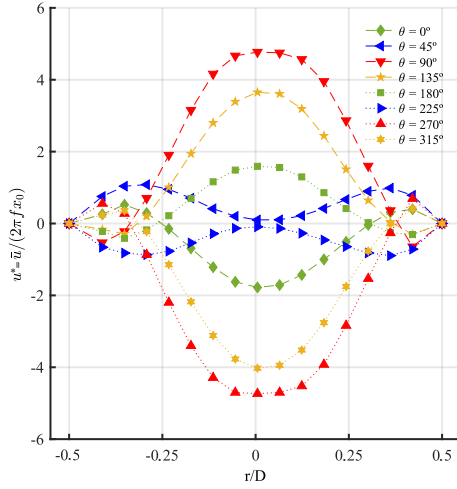
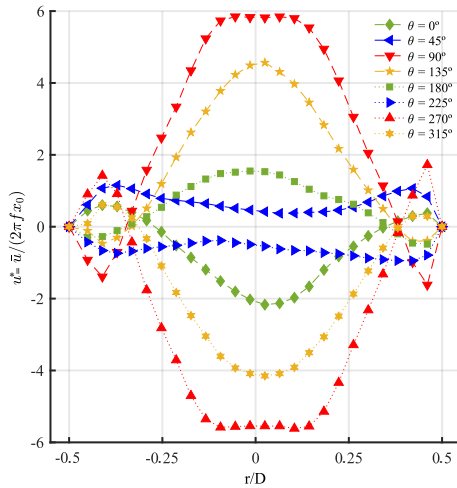


Figure 10: Phase-averaged velocity field for different instants of the oscillation cycle. Pure oscillatory flow.

patterns agree with the observation using hydrogen bubbles, but PIV results provide resolution and quantification of the different effects. For example, for positions $\theta = 0^\circ, 90^\circ, 135^\circ$, the size of the central jet (about $0.5D$) and the recirculations are observed. Besides, the representation for $\theta = 45^\circ$ shows the flow pattern after the oscillation cycle has started. At this point a jet is developing downstream of the baffles, but the flow pattern in the cell tank is dominated by low velocities in the core region of the flow and high velocities in the peripheral region, most probably due to inertial forces. This structure disappears for $\theta = 90^\circ$, where velocities in the outer region have changed their direction due to the effect of the central jet.



(a) $Re_{osc} = 51$.



(b) $Re_{osc} = 175$.

Figure 11: Phase-averaged velocity profiles at the middle cross section of a cell tank for different instants of the oscillation cycle. Pure oscillatory flow.

Fig. 11a presents the velocity profile at the middle cross section of the cell tank for 8 phase positions of the oscillation cycle. It can be observed that for $\theta = 0^\circ$ the core flow is still governed by the central jet due to

the flow inertia, with relatively high negative velocities in the central region, while the flow recirculations show velocities of the same order of magnitude. A similar behaviour was observed by Zheng et al. [28] at $Re_{osc} = 180$ and $x_0/D = 0.08$. For $\theta = 45^\circ$ all the axial velocity profile takes slightly positive values and increases with θ up to more than four times the maximum bulk velocity for $\theta = 90^\circ$. Besides it presents a symmetrical behaviour for $180^\circ < \theta < 360^\circ$.

As an example of the experiments for higher oscillatory Reynolds numbers, Fig. 11b presents the equivalent results for $Re_{osc} = 175$. They show a similar average behaviour of the flow to the case with a lower Re_{osc} : flow field dominated by the alternative creation of a jet in the core flow region and recirculations on the outer flow region. Apart from the different nature of the flow, which is not time periodic nor axisymmetric, the flow velocity is also different. As shown in Fig. 11a, the velocities for $Re_{osc} = 175$ are in general higher than for $Re_{osc} = 51$, presenting maximum velocities of 6 times the maximum average velocity of the cycle, again for $\theta = 90^\circ$.

3.2. Compound flow

The object of study in this section is the compound flow inside the baffled tube, meaning that an oscillatory flow is superimposed on a net flow. To that end, the standard Reynolds number for flow in tubes is used. To avoid misunderstanding, from here on it will be referred to as the net flow Reynolds number, Re_n .

Besides, the ratio between the Reynolds numbers of the oscillatory flow and the net flow (velocity ratio) is used as well,

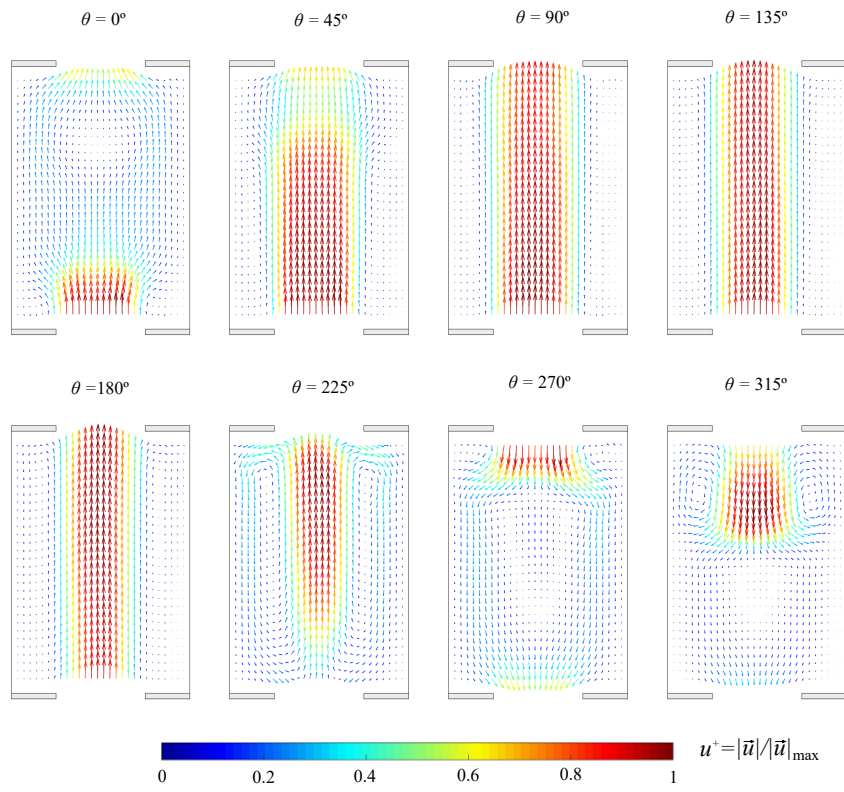
$$\Psi = \frac{Re_{osc}}{Re_n} = \frac{2\pi f x_0}{U_n} \quad (5)$$

The flow behaviour in this section is analysed by flow pattern visualization (Section 3.2.1) and heat transfer measurements (Section 3.2.2).

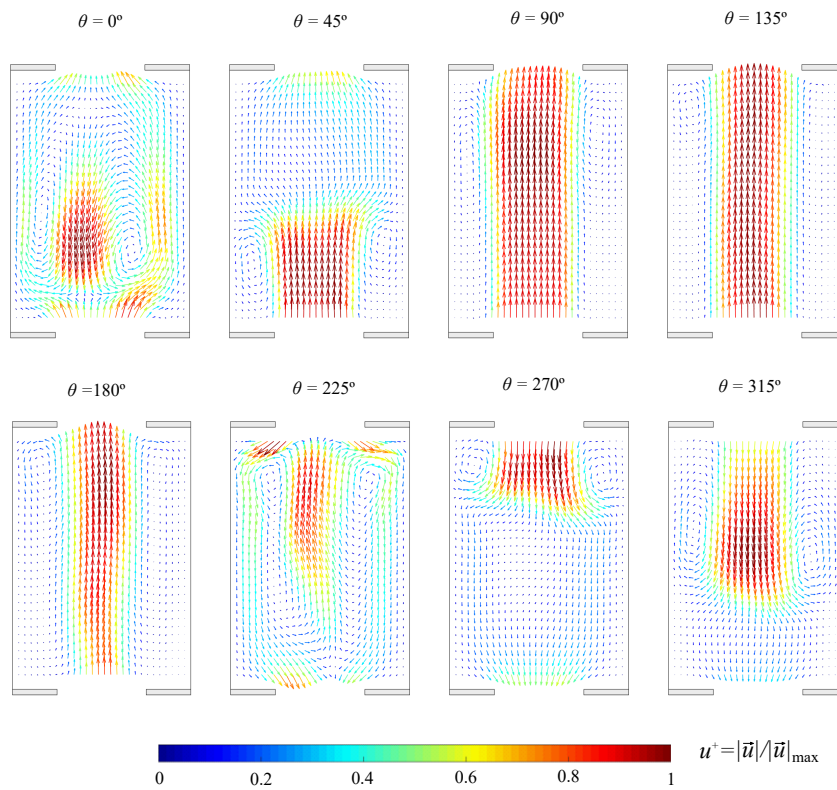
3.2.1. Flow pattern

The analysis of the superimposed net and oscillatory flows requires the evaluation of the velocity ratio, Ψ . To that end, experiments have been carried out for $Re_n = 34$ while varying the oscillatory flow in the range $1.5 < \Psi < 5$.

Fig. 12a shows the phase-averaged velocity fields at 8 phase positions for a periodic flow $Re_{osc} = 51$ and $\Psi = 1.5$. In comparison with the flow pattern observed for a pure oscillatory flow (Fig. 10 a), the flow is very similar, but presents no temporal symmetry between the positive and negative oscillation half cycles. As can be observed, the compound flow runs in the direction of the net flow (forwards) longer than in the opposite direction (backwards). Consequently, the central flow jet covers the full cell space during a significant portion of the oscillation cycle $\theta = 90^\circ, 135^\circ, 180^\circ$ in forward direction, while the recirculation vortices observed in backward direction $\theta = 315^\circ$ do not move along the full cell space.



(a) $\Psi = 1.5$ ($Re_{osc} = 51$)



(b) $\Psi = 3.7$ ($Re_{osc} = 175$)

Figure 12: Phase-averaged velocity field of a compound flow for $Re_n = 34$. Net flow direction: upwards.

This would most probably result in unsatisfactory mixing in radial direction during this part of the cycle.

Fig. 12b shows, for the same net flow Reynolds number, the phase-averaged velocity fields for a higher oscillatory Reynolds number $Re_{osc} = 175$ and $\Psi = 3.5$. As can be observed, the similarity of the flow pattern to the one of the pure oscillatory flow is higher, for higher values of Ψ . For this case, the effect of the net flow is still evident, and the forwards flow lasts longer than the backwards one. However, flow mixing during the backwards flow is much higher than for $\Psi = 1.5$.

In addition, the effect of the Reynolds numbers in the compound flow maintaining the same velocity ratio (Ψ) has been studied. For that, experiments for $\Psi = 1.7$ have been carried out while simultaneously varying both Reynolds numbers $Re_{osc} \in [51, 90]$ and $Re_n \in [28, 54]$. Results for the phase position $\theta = 225^\circ$ are shown in Fig. 13. As can be observed, the flow field is time-periodic for the case with $Re_{osc} = 51$, while the periodicity is lost for the experiment with $Re_{osc} = 90$ and the flow becomes unstable, which will increase mass transfer in radial direction.

Finally, the mixing intensity of the flow is analysed through the use of axial-radial velocity ratio proposed by Manninen et al. [18],

$$\bar{R}_v = \left[\sum_{i=1}^{n_s} \frac{1}{R_v(t_i)} \right]^{-1} \quad (6)$$

where n_s is the number of image pairs acquired during an oscillatory cycle and R_v is defined as

$$R_v(t_i) = \sum_{j=1}^{n_w} \frac{|u_j(t_i)| \cdot r_j}{|v_j(t_i)| \cdot r_j} \quad (7)$$

where r_j is the distance from the interrogation area (IA) center to the pipe axis and n_w is the number of IAs for which the corresponding velocity vector has been calculated.

A value of $\bar{R}_v < 3.5$ has been found to guarantee a good mixing [9].

Fig. 14a presents the axial-radial velocity ratio \bar{R}_v for two values of the net Reynolds number. For both cases, when the flow velocity ratio is low, $\Psi = 1$, the axial-radial velocity ratio is far over 3.5, indicating a poor mixing. Nonetheless, as the oscillation becomes more important (increasing Ψ), flow mixing increases significantly. Thus, a proper mixing ($\bar{R}_v < 3.5$) is achieved for the experiments with $Re_n = 27$ at $\Psi = 4.5$ and for $Re_n = 55$ at $\Psi \approx 2$. It can be then concluded that increasing the flow velocity ratio and/or increasing both Reynolds numbers, enhances mass transfer in radial direction.

The same results of the axial-radial velocity ratio \bar{R}_v , together with the results of a pure oscillatory flow, are plotted in Fig. 14b in order to observe the isolated effect of the oscillatory Reynolds number. These results can be compared with those provided by Fitch et al. [9],

they obtained the values of $\bar{R}_v \approx 4$ and $\bar{R}_v \approx 3$, for a $Re_{osc} = 50$ and a $Re_{osc} = 150$, respectively, in comparison with the values of $\bar{R}_v \approx 5.5$ and $\bar{R}_v \approx 3$ obtained from our experiments. The level of agreement is acceptable if we take into account that Fitch et al. tested a quite different dimensionless amplitude, $x_0/D = 0.08$. The highly decreasing trend of the axial-radial velocity ratio with the oscillatory Reynolds number and the plateau at high oscillatory Reynolds numbers was also observed by Fitch et al. [9] and Manninen et al. [18].

The main conclusion which can be extracted is that a proper mixing in radial direction is obtained for oscillatory Reynolds numbers above 130. Thus, as pointed out by Stonestreet and Van Der Veecken [26], the axial mixing is not only a function of the flow velocity ratio Ψ , but also of the Reynolds numbers. The results of this study show that only with both an oscillatory Reynolds number $Re_{osc} > 130$ and a flow velocity ratio $\Psi > 2$ a proper mixing level can be guaranteed.

3.2.2. Heat transfer

All heat transfer tests have been performed for the same Prandtl number, $Pr = 150$, and oscillation amplitude, $x_0/D = 0.5$. For each net Reynolds number tested, the Rayleigh number is kept constant and the oscillatory Reynolds number is modified. The three net Reynolds numbers tested are in the laminar flow regime, $Re_n < 170$, according to previous studies [19].

Local Nusselt number. The visualization results for the pure oscillatory flow and the compound flow have shown that the flow patterns change with time (throughout the oscillation cycle) and space (along the cell tank). Previous results have studied the local Nusselt number variation in baffle geometries under steady flow conditions [12], showing a strong dependence on the net Reynolds number.

The thermocouples arrangement allows us to obtain the local Nusselt number, based on the average wall temperature at each of the eight measuring cross-sections. In Fig. 15 the local Nusselt number is plotted as a function of the dimensionless axial distance (measured as the number of diameters from the position of the baffle previous to the measuring sections), for $Re_n = 65$ and a total number of four different oscillatory Reynolds numbers. The relative position of the baffles is indicated by vertical dashed lines.

The solution for the steady case ($Re_{osc} = 0$) is presented in Fig. 15a. As can be noticed, the distribution has an inverted U-shaped pattern: downstream of the baffles, the local Nusselt number increases progressively until it reaches a maximum. This region is associated with a separation and reattachment flow structure [19]. Once the flow is fully adhered to the wall, the boundary layer thickness increases in the axial flow direction, which yields a progressive reduction of the Nusselt number.

Another aspect to note is that the local variation in the Nusselt number along the cell tank decreases with Re_{osc}

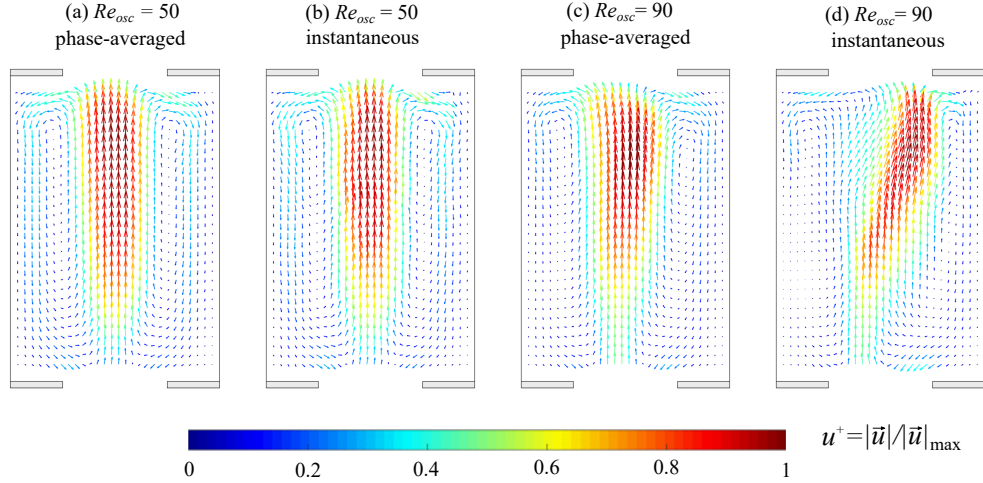


Figure 13: Velocity field of a compound flow with $\Psi = 1.7$ and $\theta = 225^\circ$ for $Re_{osc} = 50$ (left) and $Re_{osc} = 90$ (right).

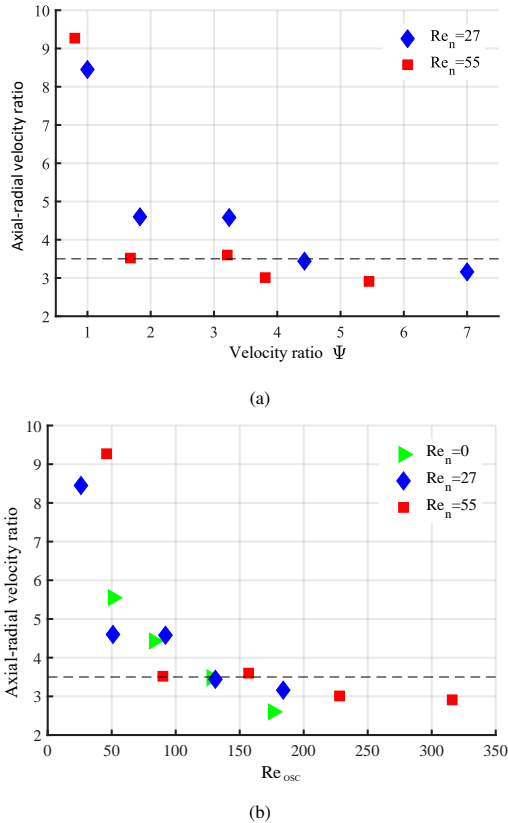


Figure 14: Axial-radial velocity ratio as a function of (a) the flow velocity ratio Ψ and (b) the oscillatory Reynolds number Re_{osc} .

for $Re_{osc} > 102$. This is in agreement with the detected change of behaviour in the visualization experiments for $Re_{osc} > 130$. In order to further quantify this trend, a parameter, which measures the mean local variation of the Nusselt number compared to the mean Nusselt number along the cell tank, is calculated. This parameter, NV_s , is obtained as:

$$NV_s = \frac{\sum_{j=1}^8 |Nu_j - \overline{Nu}|}{8 \overline{Nu}} \quad (8)$$

and can be considered as a measurement of the uniformity of the Nusselt number distribution.

The parameter is plotted in Fig. 16 as a function of the oscillatory Reynolds number for the three net Reynolds numbers tested. The three cases show the same trend, from a value corresponding to the steady case there is an increase on the Nusselt number variation, reaching the maximum at $Re_{osc} = 100 - 130$. Above this critical value the variation decreases asymptotically to a value of 5-10% at $Re_{osc} > 400$. These results are once again in agreement with the flow regimes which have been detected in the visualization results.

Unexpectedly, for low values of Re_{osc} the oscillatory flow superposition leads to an increase of the local Nusselt number variation (Fig. 16). This can also be observed in Fig. 15b, $Re_{osc} = 102$: the laminar flow oscillation implies a significant increase of the local Nusselt number at the cell tank center, while the shadow effect caused by the baffles is augmented. This effect is also observed in hydrogen bubbles experiments, where flow velocity is very low (see [Video 1 and] Fig. 7c).

As shown previously by the visualization results, above an oscillatory Reynolds number $Re_{osc} > 130$, the flow becomes chaotic [15] by the effect of the oscillatory flow. The intense mixing during both oscillation half cycles causes a more uniform local Nusselt number along the cell tank.

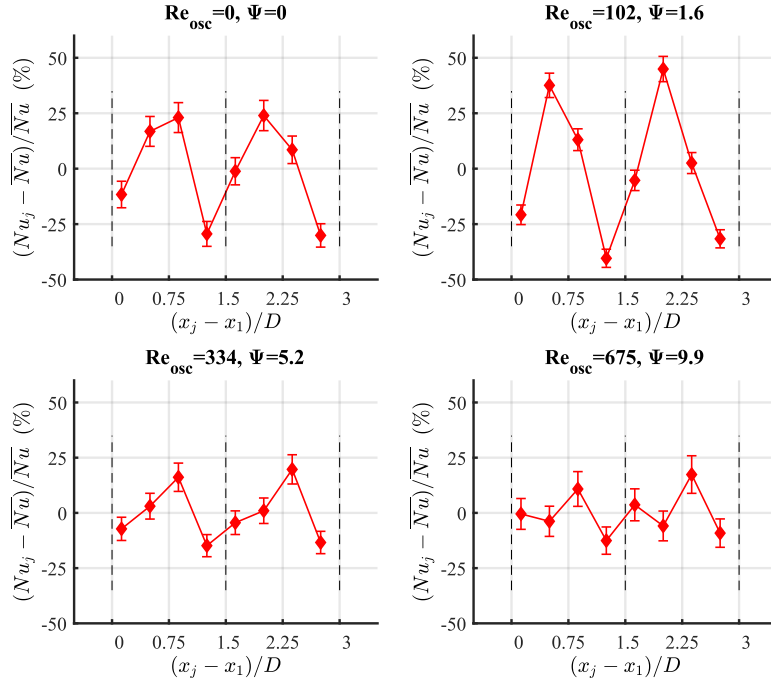


Figure 15: Local Nusselt number vs dimensionless axial distance for $Re_n = 65$, $Pr = 150$. (a) $Re_{osc} = 0$, (b) $Re_{osc} = 102$, (c) $Re_{osc} = 334$, (d) $Re_{osc} = 675$.

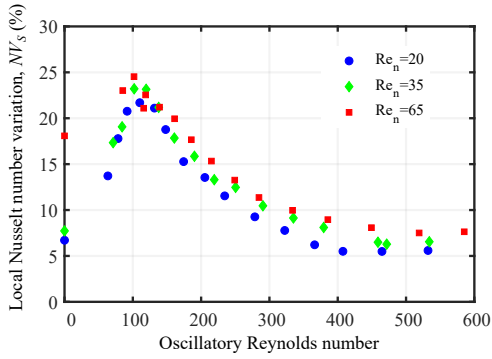


Figure 16: Local Nusselt number variation as a function of the oscillatory Reynolds number.

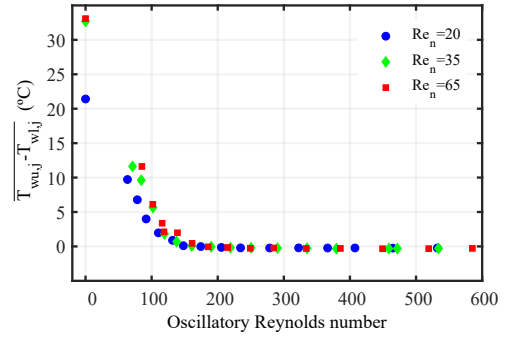


Figure 17: Mean difference between the upper and lower thermocouples as a function of the oscillatory Reynolds number.

Thermal stratification.

The experimental arrangement also allows for the study of the potential existence of mixed convection. The parameter used to quantify the buoyancy effect is the difference between the upper and lower inner wall temperatures, which is averaged along the eight measuring sections.

The average temperature difference is plotted in Fig. 17 as a function of the oscillatory Reynolds number. As can be observed, for the three steady cases ($Re_{osc} = 0$) the stratification effect is evident, with differences of around 20-30 °C between the upper and lower wall temperature. The tests for each net Reynolds number have been performed with a different heat flux and, consequently, a different Rayleigh number, so no conclusions shall be obtained about the effect of the net

Reynolds number on the stratification.

When the oscillatory flow is superimposed there is a clear progressive reduction of the temperature difference, which has already been observed in tri-orifice baffled tubes at low Reynolds numbers [20]. The temperature difference becomes negligible at an oscillatory Reynolds number of $Re_{osc} \approx 130 - 150$ and above. This limit value is very similar to the critical oscillatory Reynolds number at which the oscillatory flow becomes chaotic. Thus, the chaotic flow is enough to cancel mixed convection for the range of Rayleigh numbers in these tests, $Ra = 5.8 \cdot 10^7 - 1.3 \cdot 10^8$.

Average Nusselt number. While the local Nusselt number provides information related to the flow behaviour, the most important variable for a proper design is the

mean average Nusselt number. In Fig. 18 the average Nusselt number is shown as a function of the oscillatory Reynolds number.

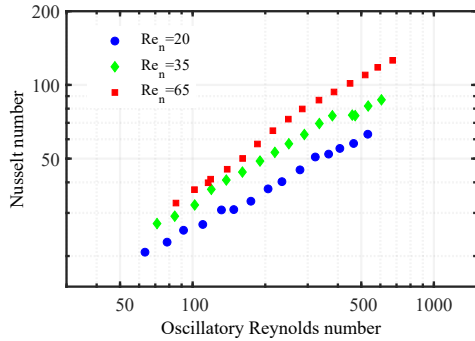


Figure 18: Average Nusselt number as a function of the oscillatory Reynolds number.

There are two main trends in the results, one is the increase in the Nusselt number when the net Reynolds number increases, and the other is the augmentation of the Nusselt number when the oscillatory Reynolds number is increased. Both trends have already been observed in baffled tubes with oscillatory flow [16, 14, 23].

However, the results cannot be compared properly with any of the three existing correlations for single orifice OBRs [16, 14, 23]. For the tested range, the extrapolation of the three correlations provides completely dissimilar results, and some of them without physical meaning (as Nusselt numbers lower than the value for a smooth tube under pure forced convection). None of these correlations has been designed for very low Reynolds numbers, but $Re_n > 100$; as a consequence, they do not consider the change in flow behaviour at low net Reynolds number, when the net flow is laminar, as has already been observed [19]. Thus, the results prove that more investigation must be done to understand the behaviour at very low net Reynolds numbers, where the OBRs can find more potential applications.

For the range of velocity ratios tested, $\Psi \leq 20$, no noticeable saturation has been observed, as the slope of the Nusselt number seems to be the same for the tested range of oscillatory Reynolds numbers. This observation agrees with the results previously reported by other studies [16, 23].

Wall temperature standard deviation. The outside wall temperature standard deviation has been used previously to distinguish the different flow regimes in smooth tubes under steady flow conditions [8]. There are 64 thermocouples along the measuring section and the mean value of the standard deviations for each thermocouple is used as the relevant parameter. In this way, we aim at quantifying the local wall temperature variation over time and not between different positions (in the axial or azimuthal direction).

However, it is reasonable to argue that for a lower temperature difference between the wall and the bulk

fluid, the standard deviation of the wall temperature would also be lower for the same flow pattern. This observation is relevant because the tests have been carried out for an approximately constant Rayleigh (same heat flux); thus, a higher oscillatory Reynolds number implies a higher convection coefficient, and, consequently, a reduction of the wall-bulk fluid temperature difference. In order to compensate for this effect, a dimensionless standard deviation of the wall-bulk temperature difference is considered:

$$\frac{\sigma(T_{wi,jk} - T_{b,j})}{\bar{T}_{wi} - \bar{T}_{b,j}} \cdot 100 \quad (9)$$

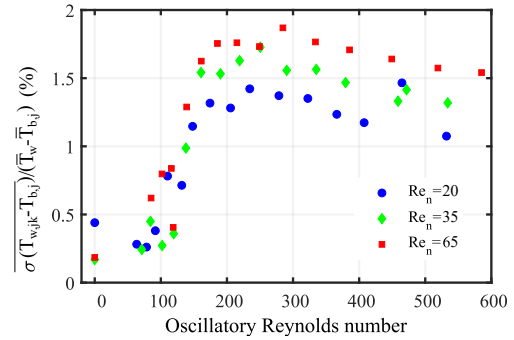


Figure 19: Dimensionless wall temperature standard deviation as a function of the oscillatory Reynolds number.

This parameter is plotted in Fig. 19. For the three net Reynolds numbers tested the values are quite low, 0.5%, for the steady flow case and for oscillatory flow Reynolds numbers $Re_{osc} < 100$. This non-zero but low value can be again justified by the repeatability of the thermocouples. Above $Re_{osc} = 100$ there is a sharp increase in the dimensionless standard deviation up to 1.5% (three times the value found in the laminar flow regime) at $Re_{osc} = 200$. This range coincides again with the critical Reynolds number at which the flow becomes chaotic, confirming that the flow behaviour has a remarkable effect on the wall temperature, caused by the deviation of the central, colder stream, which moves towards the walls and increases the wall temperature variation.

In the higher range of oscillatory Reynolds numbers tested ($Re_{osc} = 200 - 600$) this value does not suffer significant changes, suggesting a flow with a similar level of chaos, or, at least, at the level at which the chaos can have an influence on the wall temperature variation over time.

4. Conclusions

- Under oscillatory flow conditions, flow axisymmetry and temporal periodicity have been observed for $Re_{osc} < 130$, pointing out a two-dimensional laminar flow behaviour. During the negative and positive half cycles, recirculations are

created downstream of the baffles and they grow along the cell length. Above $Re_{osc} \approx 130$, the flow becomes asymmetric and three-dimensional.

- The effect of increasing the velocity ratio (Ψ) or the oscillatory Reynolds number is to increase the mixing intensity (reducing the axial-radial velocity ratio, $\overline{R_v}$). To achieve an appropriate mixing ($\overline{R_v} < 3.5$), a high enough oscillatory Reynolds number, $Re_{osc} \geq 130$, is required, in addition to a high velocity ratio ($\Psi \geq 2$).
- Both net and oscillatory Reynolds numbers have a positive impact on the Nusselt number. In the range tested, up to 3-5 times increases on the heat transfer rate have been measured in comparison to the steady flow case. No saturation of the heat transfer rate has been detected for the range of velocity ratios tested ($\Psi < 20$).
- The results have shown a close connection between the local Nusselt number (along a cell tank) and the flow structure, with a more uniform Nusselt number distribution when the oscillatory flow becomes chaotic, $Re_{osc} \approx 130$.
- The existence of mixed convection has been observed under laminar steady flow conditions and with a superimposed oscillatory for $Re_{osc} < 150$. The onset of the chaotic oscillatory flow removes the thermal stratification of the flow.
- The onset of the chaotic flow regime has a significant effect on the standard deviation of the wall temperature over time. There is a sharp increase of this value in the range $100 < Re_{osc} < 200$.

Acknowledgments

The authors gratefully acknowledge the financial support of the project DPI2015-66493-P by Ministerio de Economía y Competitividad (MINECO, Spain) and the European Regional Development Fund (ERDF).

References

- [1] Amiri, S., Taher, R., Mongeau, L., 2017. Quantitative visualization of temperature field and measurement of local heat transfer coefficient over heat exchanger elements in sinusoidal oscillating flow. *Experimental Thermal and Fluid Science* 85, 22 – 36. doi:<https://doi.org/10.1016/j.expthermflusci.2017.02.008>.
- [2] ASHRAE, 2001. ASHRAE fundamentals handbook.
- [3] Özer Bağcı, Dukhan, N., 2018. Impact of pore density on oscillating liquid flow in metal foam. *Experimental Thermal and Fluid Science* 97, 246 – 253. doi:<https://doi.org/10.1016/j.expthermflusci.2018.04.020>.
- [4] Bejan, A., Kraus, A.D., 2003. Heat transfer handbook.
- [5] Brunold, C.R., Hunns, J.C.B., Mackley, M.R., Thompson, J.W., 1989. Experimental observations on flow patterns and energy losses for oscillatory flow in ducts containing sharp edges. *Chemical Engineering Science* 44, 1227–1244. doi:[https://doi.org/10.1016/0009-2509\(89\)87022-8](https://doi.org/10.1016/0009-2509(89)87022-8).
- [6] Churchill, S., Chu, H., 1975. Correlating equations for laminar and turbulent free convection from a horizontal cylinder. *International Journal of Heat Mass Transfer* 18, 1049–1053.
- [7] Dunn, P., Davis, M., 2018. Measurement and data analysis for engineering and science. 4th ed.,
- [8] Everts, M., Meyer, J., 2018. Heat transfer of developing and fully developed flow in smooth horizontal tubes in the transitional flow regime. *International Journal of Heat and Mass Transfer* 117, 1331–1351.
- [9] Fitch, A.W., Jian, H., Ni, X., 2005. An investigation of the effect of viscosity on mixing in an oscillatory baffled column using digital particle image velocimetry and computational fluid dynamics simulation. *Chemical Engineering Journal* 112, 197–210. doi:10.1016/j.cej.2005.07.013.
- [10] Jian, H., Ni, X., 2005. A numerical study on the scale-up behaviour in oscillatory baffled columns. *Chemical Engineering Research and Design* 83, 1163–1170. doi:10.1205/cherd.03312.
- [11] Kamsanam, W., Mao, X., Jaworski, A.J., 2015. Development of experimental techniques for measurement of heat transfer rates in heat exchangers in oscillatory flows. *Experimental Thermal and Fluid Science* 62, 202 – 215. doi:<https://doi.org/10.1016/j.expthermflusci.2014.12.008>.
- [12] Kiml, R., Magda, A., Mochizuki, S., Murata, A., 2004. Rib-induced secondary flow effects on local circumferential heat transfer distribution inside a circular rib-roughened tube. *International Journal of Heat and Mass Transfer* 47, 1403–1412. doi:10.1016/j.ijheatmasstransfer.2003.09.026.
- [13] Kutz, M., 2006. Heat Transfer Calculations.
- [14] Law, R., Ahmed, S., Tang, N., Phan, A., Harvey, A., 2018. Development of a more robust correlation for predicting heat transfer performance in oscillatory baffled reactors. *Chemical Engineering and Processing: Process Intensification* 125, 133–138.
- [15] Mackay, M., Mackley, M., Y., W., 1991. Oscillatory flow within tubes containing wall or central baffles. *Trans IChemE* 69, 506–513.
- [16] Mackley, M.R., Stonestreet, P., 1995. Heat transfer and associated energy dissipation for oscillatory flow in baffled tubes. *Chemical Engineering* 50, 2211–2224.
- [17] Mackley, M.R., Tweddle, G.M., Wyatt, I.D., 1990. Experimental heat transfer measurements for pulsatile flow in baffled tubes. *Chemical Engineering Science* 45, 1237–1242. doi:10.1016/0009-2509(90)87116-A.
- [18] Manninen, M., Gorshkova, E., Immonen, K., Ni, X.W., 2013. Evaluation of axial dispersion and mixing performance in oscillatory baffled reactors using CFD. *Journal of Chemical Technology & Biotechnology* 88, 553–562. doi:10.1002/jctb.3979.
- [19] Muñoz-Cámara, J., Crespí-Llorens, D., Solano, J., Vicente, P., 2020a. Experimental analysis of flow pattern and heat transfer in circular-orifice baffled tubes. *International Journal of Heat and Mass Transfer* 147, 118914. doi:10.1016/j.ijheatmasstransfer.2019.118914.
- [20] Muñoz-Cámara, J., Solano, J., Pérez-García, J., 2020b. Experimental correlations for oscillatory-flow friction and heat transfer in circular tubes with tri-orifice baffles. *International*

[21] Ni, X., Jian, H., Fitch, A., 2002. Computational fluid dynamic modelling of flow patterns in an oscillatory baffled column. *Chemical Engineering Science* 57, 2849–2862. doi:10.1016/S0009-2509(02)00081-7.

[22] Ni, X., Mackley, M., Harvey, A., Stonestreet, P., Baird, M., Rama Rao, N., 2003. Mixing Through Oscillations and Pulsations—A Guide to Achieving Process Enhancements in the Chemical and Process Industries. *Chemical Engineering Research and Design* 81, 373–383. doi:10.1205/02638760360596928.

[23] Paste Particle and Polymer Processing group (P4G), . <https://www.ceb.cam.ac.uk/research/groups/rg-p4g/archive-folder/pfg/ofm-folder/ofm-advantages-enhancement-of-heat-transfer-rates>.

[24] Smith, K., Mackley, M., 2006. An experimental investigation into the scale-up of oscillatory flow mixing in baffled tubes. *Chemical Engineering Research and Design* 84, 1001–1011.

[25] Smith, K.B., 1999. The Scale-Up of Oscillatory Flow Mixing. Ph.D. thesis.

[26] Stonestreet, P., Van Der Veecken, P.M., 1999. The effects of oscillatory flow and bulk flow components on residence time distribution in baffled tube reactors. *Chemical Engineering Research and Design* 77, 671–684. doi:10.1205/026387699526809.

[27] Thielicke, W., Stamhuis, E.J., 2014. PIVlab – Towards User-friendly, Affordable and Accurate Digital Particle Image Velocimetry in MATLAB. *Journal of Open Research Software* 2, 1–10. doi:10.5334/jors.b1.

[28] Zheng, M., Li, J., Mackley, M.R., Tao, J., 2007. The development of asymmetry for oscillatory flow within a tube containing sharp edge periodic baffles. *Physics of Fluids* 19, 1–15. doi:10.1063/1.2799553.

List of Figures

1	Baffle geometry and thermocouple arrangement in the test section.	3
2	(a) Visualization facility, (b) image acquisition setup for hydrogen bubbles experiments and (c) PIV experiments. Visualization facility parts: (1) centrifugal pump, (2) flow control valve, (3) P100 inlet, (4) baffles, (5) PT100 outlet, (6) manual valve, (7) plate heat exchanger, (8) chiller, (9) Coriolis flowmeter, (10) reservoir tank, (11) electric heater, (12) gear-motor assembly, (13) connecting rod-crank, (14) hydraulic cylinder, (15) magnetostrictive position sensor.	4
3	Instantaneous volumetric flow rate obtained from the PIV velocity field. . . .	5
4	Heat transfer facility setup. (1) Main Tank, (2) positive displacement pumping system, (3) Coriolis flowmeter, (4) input flow temperature probe B 1/10 DIN PT100, (5) insert baffles, (6) type T thermocouples set, (7) output flow temperature probe, (8 and 9) manually operated valves, (10) autotransformer, (11) double effect hydraulic piston, (12) connecting rod-crank, (13) gear-motor assembly, (14) magnetostrictive position sensor, (15) agitator.	7
5	Temperature variation along the test section.	7
6	Phases of the oscillation cycle for flow field representation (PIV technique). . .	8
7	Front view of the hydrogen bubble seeded plane for $Re_{osc} = 32$. (a) $\theta = -22^\circ$, (b) $\theta = 22^\circ$, (c) $\theta = 55^\circ$ y (d) $\theta = 90^\circ$. $x_0/D = 0.5$	8
8	Lateral view of the hydrogen bubble seeded plane for instant $\theta = 180^\circ$, for (a) $Re_{osc} = 32$ y (b) $Re_{osc} = 150$. $x_0/D = 0.5$	9
9	Phase-averaged vs. instantaneous velocity fields. Pure oscillatory flow . . .	10
10	Phase-averaged velocity field for different instants of the oscillation cycle. Pure oscillatory flow.	10
11	Phase-averaged velocity profiles at the middle cross section of a cell tank for different instants of the oscillation cycle. Pure oscillatory flow.	11
12	Phase-averaged velocity field of a compound flow for $Re_n = 34$. Net flow direction: upwards.	12
13	Velocity field of a compound flow with $\Psi = 1.7$ and $\theta = 225^\circ$ for $Re_{osc} = 50$ (left) and $Re_{osc} = 90$ (right).	14

14	Axial-radial velocity ratio as a function of (a) the flow velocity ratio Ψ and (b) the oscillatory Reynolds number Re_{osc} .	14
15	Local Nusselt number vs dimensionless axial distance for $Re_n = 65$, $Pr = 150$. (a) $Re_{osc} = 0$, (b) $Re_{osc} = 102$, (c) $Re_{osc} = 334$, (d) $Re_{osc} = 675$.	15
16	Local Nusselt number variation as a function of the oscillatory Reynolds number.	15
17	Mean difference between the upper and lower thermocouples as a function of the oscillatory Reynolds number.	15
18	Average Nusselt number as a function of the oscillatory Reynolds number.	16
19	Dimensionless wall temperature standard deviation as a function of the oscillatory Reynolds number.	16